Supplementary information

Title: Luminescent Surfaces with Tailored Angular Emission for Compact Dark-Field Imaging Devices

Authors: Cécile A. C. Chazot[1], Sara Nagelberg[1], Christopher J. Rowlands[2], Maik R. J. Scherer[3], Igor Coropceanu[4], Kurt Broderick[5], Yunjo Kim[1], Moungi G. Bawendi[4], Peter So[1], and Mathias Kolle[1]*

[1] Mechanical Engineering Department, Massachusetts Institute of Technology, 77 Massachusetts Avenue, Cambridge, Massachusetts, 02139, United States of America.

[2] Department of Bioengineering, Imperial College London, South Kensington, SW7 2AZ, UK

[3] Papierfabrik Louisenthal GmbH, Louisenthal 1, Gmund am Tegernsee, 83703, Germany

[4] Department of Chemistry, Massachusetts Institute of Technology, 77 Massachusetts Avenue, Cambridge, Massachusetts, 02139, United States of America.

[5] Microsystems Technology Laboratory, Massachusetts Institute of Technology, 60 Vassar Street, Cambridge, Massachusetts, 02139, United States of America.

Modelling image formation for trans-illuminated phase objects in SLED or bright-field light

To theoretically assess image formation in a microscope system under bright-field or dark field illumination, the partial coherence of the illumination needs to be taken into account. The theoretical framework for imaging with a partially coherent optical system was first discussed by Hopkins in 1953[1] and is treated comprehensively in textbooks by Born and Wolf[2] and Goodman[3]. Here, we outline how the theory of imaging with partially coherent light was applied to characterize the effect of the SLED surface as compared to standard bright-field illumination on image formation with a phase object in a 4-f system. In the following, we assume quasi-monochromatic illumination. This is a justifiable approximation for the SLED surfaces given the narrow emission band of the quantum dots. It also holds for the bright-field illumination resulting from the light that is specularly reflected by the Bragg reflector. For an optical system with quasi-monochromatic, spatially partially coherent illumination, the quantity that describes the system's image formation characteristics is the mutual intensity or its normalized equivalent, the complex

degree of spatial coherence. The illumination configuration implemented with the SLED surfaces is spatially uniform in intensity and is akin to Köhler's illumination, whether the SLED surface emission or the spectrally selective specular reflection from the SLED surface's Bragg reflector (bright-field) are used for object plane illumination. Under these circumstances, the complex degree of spatial coherence for two points in the object plane (x_1, y_1) and (x_2, y_2) depends only on the coordinate differences, i.e. $j(x_1, x_2, y_1, y_2) = j(x_2 - x_1, y_2 - y_1)$ and it is proportional to the Fourier transform of the angular spectrum of the illumination[1,2]. Specifically, for bright-field illumination achieved through the spectrally selective specular reflection of incident light from the SLED surface's Bragg reflector, the angular spectrum (Fig. S1a, b) as a function of spatial frequencies (u, v) is

$$\mathcal{J}_{\mathrm{bf}}\big(\mathrm{u}(\theta,\varphi), \mathrm{v}(\theta,\varphi)\big) = \begin{cases} 1, & \sqrt{\mathrm{u}(\theta,\varphi)^2 + \mathrm{v}(\theta,\varphi)^2} \leq \frac{\mathrm{NA}}{\lambda_0} \\ 0, & \text{otherwise} \end{cases}$$

with $\mathrm{u}(\theta,\varphi) = \frac{n}{\lambda_0} \cdot \sin\theta \cos\varphi$ and $\mathrm{v}(\theta,\varphi) = \frac{n}{\lambda_0} \cdot \sin\theta \sin\varphi$, where n is the refractive index of the surrounding medium, θ is the polar angle, φ the azimuthal angle and $\lambda_0 = 630\mathrm{nm}$ the wavelength at the center of the surface's emission / reflection peak.

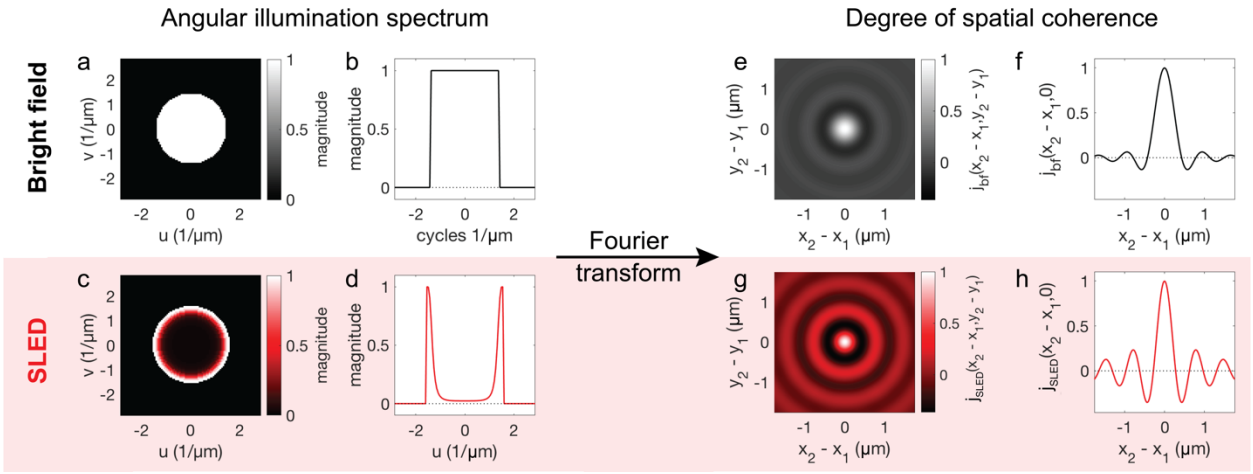

Figure S1: **Angular illumination spectra and degree of spatial coherence.** a, b) Magnitude map of the angular spectrum of the bright-field illumination as a function of spatial frequencies u and v and profile of the angular spectrum at $\mathrm{v} = 0\ \mu\mathrm{m}^{-1}$. c, d) Same as (a, b) for SLED illumination. The frequency cut-off is at $\sqrt{\mathrm{u}^2 + \mathrm{v}^2} = \frac{\mathrm{NA}}{\lambda_0}$. e, f) Map of the degree of spatial coherence $j_{\mathrm{bf}}(x_2 - x_1, y_2 - y_1)$ and its profile at $y_2 - y_1 = 0\mu\mathrm{m}$. g, h) Same as (e, f) for SLED illumination.

For illumination of the object using the fluorescent emission of the SLED surface the angular spectrum (Fig. S1c, d) is

$$\mathcal{J}_{\mathrm{SLED}}\big(\mathrm{u}(\theta,\varphi),\mathrm{v}(\theta,\varphi)\big) = \sqrt{E(\theta,\lambda_0)}\,,$$

where the angle- and wavelength-dependent emission of the SLED surface $E(\theta,\lambda)$ is given by $E(\theta,\lambda_0) = T(\theta,\lambda_0)\cdot E_{\mathrm{QD}}(\lambda_0)$, where $T(\theta,\lambda_0)$ describes the transmission of light by the Bragg-reflector and $E_{\mathrm{QD}}(\lambda_0)$ the emission spectrum of the quantum dots (see Fig. 1c in the main text). With the quantum dot emission spectrum being reasonably narrow, the calculus below will be restricted to the quantum dot emission centre wavelength $\lambda_0 = 630\mathrm{nm}$.

The Fourier transforms of $\mathcal{J}_{\mathrm{bf}}$ and $\mathcal{J}_{\mathrm{SLED}}$ are proportional to the degrees of spatial coherence $j_{\mathrm{bf}}(x_2-x_1,y_2-y_1)$ for bright-field (Fig. S1e, f) and $j_{\mathrm{SLED}}(x_2-x_1,y_2-y_1)$ for SLED illumination (Fig. S1g, h):

$$j_{\mathrm{bf}}(x_2-x_1,y_2-y_1) = \frac{2\cdot J_1\left(2\pi\frac{NA}{\lambda_0}\sqrt{(x_2-x_1)^2+(y_2-y_1)^2}\right)}{2\pi\frac{NA}{\lambda_0}\sqrt{(x_2-x_1)^2+(y_2-y_1)^2}}$$

$$j_{\mathrm{SLED}}(x_2-x_1,y_2-y_1) = \int_0^{2\pi}\int_0^{\frac{\pi}{2}} \sqrt{E(\theta,\lambda_0)}\cdot \mathrm{e}^{2\pi i\frac{n}{\lambda_0}\sin\theta\cdot[\cos\varphi\cdot(x_2-x_1)+\sin\varphi\cdot(y_2-y_1)]}\mathrm{d}\theta\mathrm{d}\varphi$$

Here J_1 is the Bessel function of the first kind and first order.

Representation of coherence effects in the illumination via the degree of spatial coherence to assess their influence on the formation of images of trans-illuminated phase objects is strictly valid only when the delay differences induced by the object are much less than the coherence time of the illumination. The coherence time τ_{c} associated with the quantum dot emission is of the order of $\tau_{\mathrm{c}} \leq \frac{1}{\Delta\nu} \approx \frac{\lambda_0^2}{c\cdot\Delta\lambda} \approx 10^{-14}\mathrm{s}$, where $\Delta\nu$ is the spectral bandwidth, $\lambda_0 = 630\mathrm{nm}$ is the peak quantum dot emission wavelength, the speed of light $c \approx 3\cdot 10^8\,\frac{\mathrm{m}}{\mathrm{s}}$, and $\Delta\lambda \approx 40\mathrm{nm}$ is the emission peak

width at half maximum (FWHM). The temporal delays expected for microscale phase objects with weak refractive index contrast to the surrounding medium are of the order of $\frac{\Delta n \cdot d}{c} \approx 10^{-17}$s to 10^{-15}s (for object thicknesses d ranging from 1µm to 50µm and refractive index contrasts Δn from 0.01 to 0.03), which is at least an order of magnitude smaller than the source's coherence time τ_c.

Having determined the degrees of spatial coherence in the object plane, we now aim to obtain the spatial degrees of coherence in the image plane after the light has interacted with the object and is transmitted through the imaging system. From this information, we can deduce the intensity distribution in the image plane.

For simplicity, we assume a 4-f system with unit magnification, which reduces the amount of scaling factors to be accounted for in the description of the propagation of light from object to image (Fig. S2).

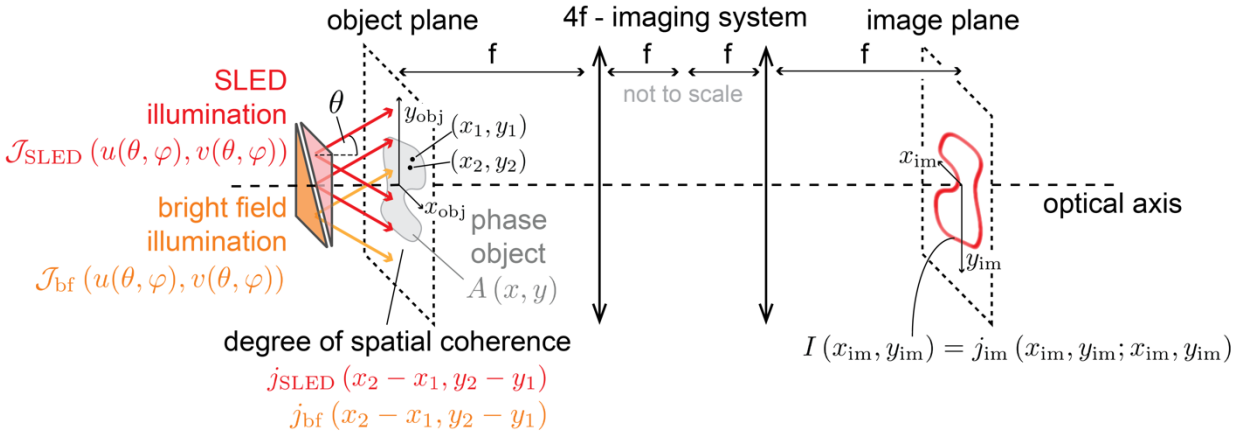

Figure S2: **Schematic of the imaging system.** Bright-field and SLED illumination are both akin to Köhler illumination, which enables us to deduce the degrees of spatial coherence j_{bf} and j_{SLED} for both illumination types from the illumination's angular spectra $\mathcal{J}_{\mathrm{bf}}$ and $\mathcal{J}_{\mathrm{SLED}}$. A phase object modifies the incident light and the intensity distribution in the image plane can be deduced from the corresponding degree of spatial coherence j_{im} in the image plane. θ is the polar angle of incident light, while φ (not shown here) describes the azimuthal angle.

For small enough objects the imaging system can be considered space-invariant (isoplanatic); its amplitude transmission function $h(x_{\mathrm{obj}}, y_{\mathrm{obj}}, x_{\mathrm{im}}, y_{\mathrm{im}})$, which describes how a disturbance at point $(x_{\mathrm{obj}}, y_{\mathrm{obj}})$ in the object plane contributes to the complex amplitude at point $(x_{\mathrm{im}}, y_{\mathrm{im}})$ in the

image plane, to a good approximation then only depends on the coordinate differences $x_{\mathrm{im}} - x_{\mathrm{obj}}$ and $y_{\mathrm{im}} - y_{\mathrm{obj}}$, i.e. $h(x_{\mathrm{obj}}, y_{\mathrm{obj}}, x_{\mathrm{im}}, y_{\mathrm{im}}) = h(x_{\mathrm{im}} - x_{\mathrm{obj}}, y_{\mathrm{im}} - y_{\mathrm{obj}})$.[2,3]

The normalized intensity $I(x_{\mathrm{im}}, y_{\mathrm{im}})$ projected by the object in the image plane can then be obtained by evaluating the image plane degree of spatial coherence at that coordinate, which is given by a four-dimensional integral:

$$I(x_{\mathrm{im}}, y_{\mathrm{im}}) = j_{\mathrm{im}}(x_{\mathrm{im}}, y_{\mathrm{im}}; x_{\mathrm{im}}, y_{\mathrm{im}})$$
$$= \iiiint_{a} j_{\mathrm{s}}(x - x', y - y')\, A(x, y) A^{*}(x', y')\, h(x_{\mathrm{im}} - x, y_{\mathrm{im}} - y) h^{*}(x_{\mathrm{im}} - x', y_{\mathrm{im}} - y')\, \mathrm{d}x\mathrm{d}x'\mathrm{d}y\mathrm{d}y'$$

Here, $j_{\mathrm{s}} = j_{\mathrm{SLED}}$ for illumination of the object with the SLED surface and $j_{\mathrm{s}} = j_{\mathrm{bf}}$ for bright-field illumination. The integration area a is the illuminated object area that is parsed by the integration variables x, y, x' and y'. $A(x, y)$ is the complex amplitude transmission function of the phase object. * marks the complex conjugates.

This theoretical assessment of image formation with partially coherent light allows us to model the SLED surfaces in comparison with bright-field illumination. The metric of comparison used here (see Fig. 5g in the main text) is the ratio of contrast r_{c} achieved with SLED light and bright-field illumination, given by

$$r_{\mathrm{c}} = \frac{c_{\mathrm{SLED}}}{c_{\mathrm{bf}}}$$

where the usual definition of contrast

$$c_{\mathrm{SLED\,/\,bf}} = \left(\frac{I_{\mathrm{max}} - I_{\mathrm{min}}}{I_{\mathrm{max}} + I_{\mathrm{min}}}\right)_{\mathrm{SLED\,/\,bf}}$$

based on the maximum and minimum intensities (I_{max}, I_{min}) in the image is used.
For the simulations presented in Fig. 5 in the main text, we used an imaging system with a numerical aperture of 1 to image a phase object with refractive index 1.37 in a medium of refractive index 1.33.

Alternatives for the bottom reflector - comparison between the spherical concavities and randomly rough surfaces

To answer the question whether bottom reflectors made from spherical concavities (Fig. S3a) are advantageous compared to a randomly roughened reflective surface (Fig. S3b), we modelled the angular emission of gold surfaces with Gaussian random height distribution and the same correlation length as the spherical concavities.

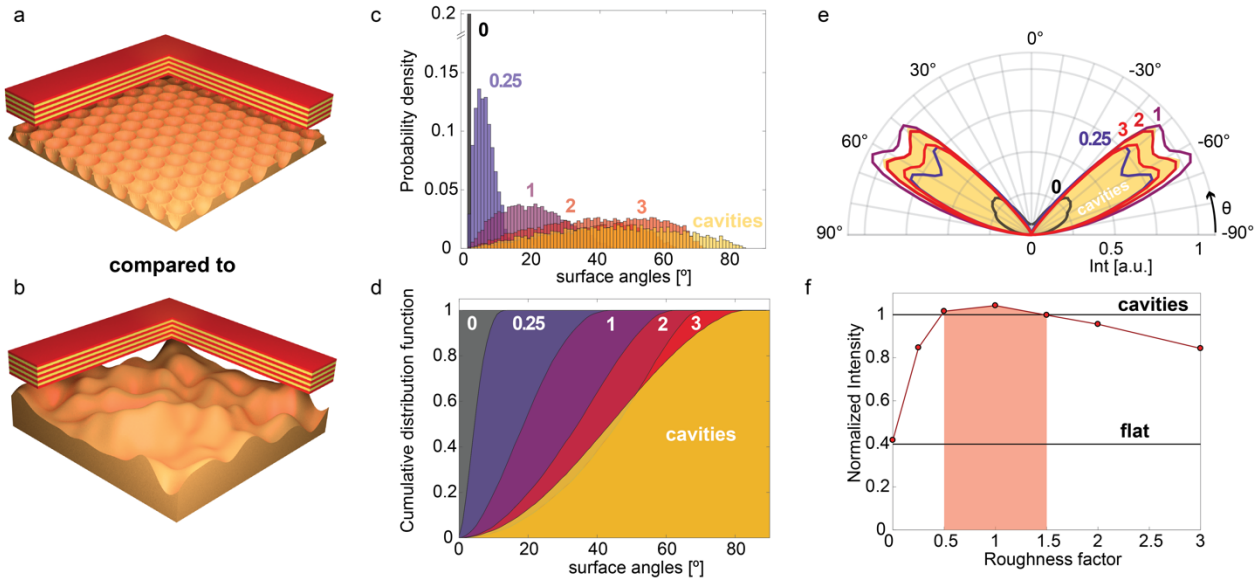

Figure S3**: Comparison of the optical performance of the semi-spherical geometries with simulated randomly generated rough surfaces.** a, b) Schematics representing the simulated spherical cavity geometry (a) and a rough surface with random Gaussian height distribution and the same correlation length of 5µm. c) Probability density function of surface normal angles for rough surfaces with zero- (grey), 0.25- (dark blue), one- (violet), two- (orange), and three-times (red) the RMS amplitude of the spherical concavities, whose surface angle probability density is shown for comparison in yellow. d) The cumulative distribution function of the probability distributions shown in (c) indicating the probability of a surface angle being smaller than or equal to any specific chosen value. e) Polar plot comparing the modelled surface's angular emission profiles for amplitudes of zero-, 0.25-, one-, two-, and three-times the RMS amplitude of the spherical concavities, whose angular emission profile is shown in the yellow shade for comparison. f) Plot of the intensity of the random rough surfaces integrated over the whole angle range and shown as a function of the roughness factor, i.e. the ratio of the surfaces' RMS amplitude to the spherical concavities' RMS amplitude. The integrated intensity values are normalized with respect to the integrated intensity of the emission from the substrates with spherical concavities as the bottom reflector, which is shown as the top black line. The intensity level of a flat bottom reflector is shown with the bottom black line. The red shading marks the range in which the random rough surfaces outperform the spherical concavity bottom reflector.

Specifically, we tested rough bottom reflector surfaces with seven different root mean square (RMS) amplitudes, amounting to between zero- to three-times of the RMS amplitude of the

spherical concavities. The probability distributions of the surface normal angles and their cumulative distribution functions are shown in Figures S3c and S3d for a selection of randomly rough surfaces in comparison to the spherical concavities. Our modelling results (summarized in the polar plot of emission intensity vs. emission angle in Fig. S3e and the integrated intensity vs. RMS surface amplitude in Fig. S3f) suggest that the rough surfaces with a RMS amplitude of 0.5- to 1.5-times that of the spherical concavities perform slightly better. Outside of this range the spherical concavities provide a higher emission intensity. Provided that randomly rough surfaces can be formed with a controlled RMS amplitude without adding fabrication complexity they could represent the preferable choice for the bottom reflector. It could also prove beneficial to decrease the rough surface's correlation length but a detailed quantitative assessment of that lies beyond the scope of this paper.

Digital contrast enhancement

Digital contrast enhancement of the bright-field images did not allow us to reveal the specimen structure anywhere nearly as well as with the SLED approach (Fig. S4).

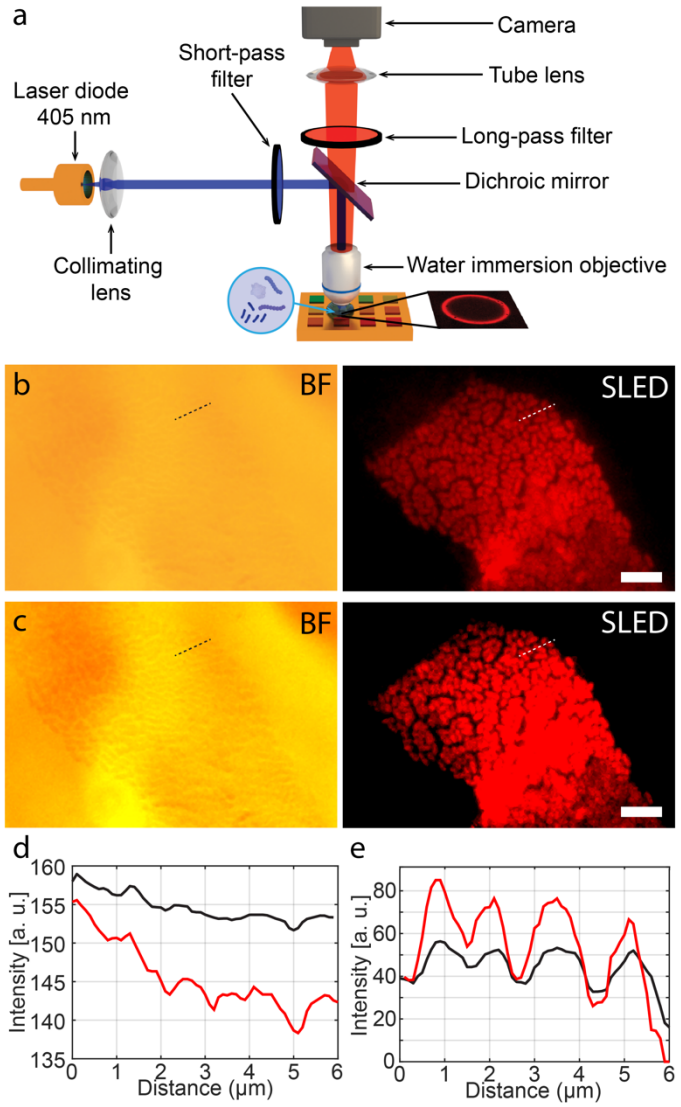

Figure S4**: Influence of increasing numerically the contrast of both bright-field and SLED images on the intensity profiles.** a) Schematics of the optical setup used for imaging. A drop of water containing *E. coli* was deposited on the surface and imaged using a water immersion lens. SLED measurements rely on exposure of the substrate with blue light from a laser diode. b, c) Comparison of standard bright-field images of *E. coli* with images obtained by SLED. b) The as-captured pictures and c) the same images after a contrast increase of 50% and brightness decrease of 20% to be able to reveal the feature on the bright-field image as much as possible.

Design variables for SLED surfaces

Provided the SLED surface has a bottom reflector that can diffusely scatter light, two key elements determine its emission characteristics: (1) the emission spectrum of the light sources embedded in the SLED surface (here the quantum dots) and (2) the transmission characteristics of the Bragg reflector, which for a given choice of materials can be tuned by altering the thickness of individual layers and the overall number of layers. For different emission spectra and Bragg reflector designs, Figure S5 shows a collection of modelled angular emission profiles accompanied by the Bragg reflector's dispersion diagram with a coloured overlay at the angle ranges at which emitted light can escape from the Bragg reflector and a plot of emitted intensity vs. emission angle. The corresponding relevant parameters for each of the data sets are shown in the matrix in Figure S6.

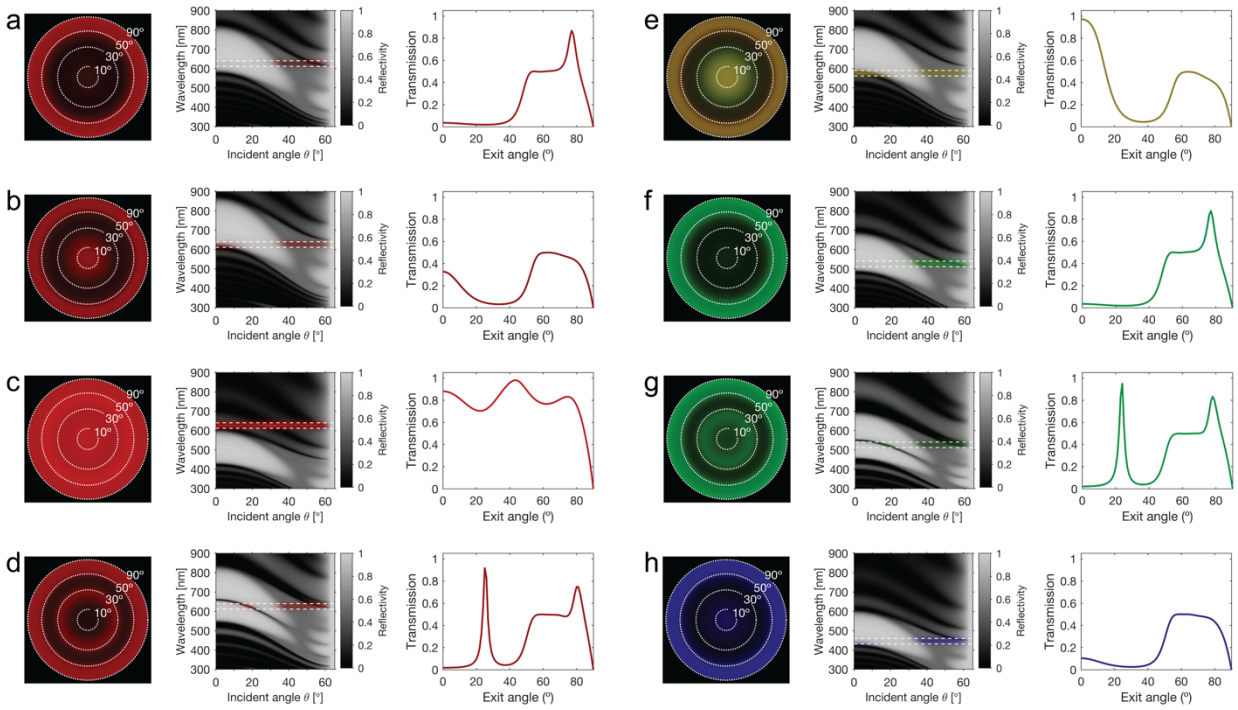

Figure S5**: Angular emission profiles, Bragg reflector characteristics and angular emitted intensity plots of different SLED surface designs.** The emission peak centre wavelengths of the SLED surfaces are 627nm for (a-d), 576nm for (e), 526nm for (f, g), and 446nm for (h). All Bragg reflectors are ideal multilayers made from alternating layers of TiO_2 (n = 2.20) and SiO_2 (n = 1.49). The total layer number is 13 for (a-c, e, f, h), while the reflection peak centre wavelength of the Bragg reflector varies: (a, e) 680nm, (b) 720nm, (c) 500nm, (f) 570nm, and (h) 500nm. The SLED surfaces corresponding to the data in (d, g) consist of two ideal Bragg stacks with nine alternating TIO_2 and SiO_2 layers. The two Bragg reflectors are deposited on top of each other to form a half-wave defect layer made from TiO_2, which creates a characteristic narrow passband in the Bragg mirror's reflection spectrum at (d) 660nm and (g) 550nm.

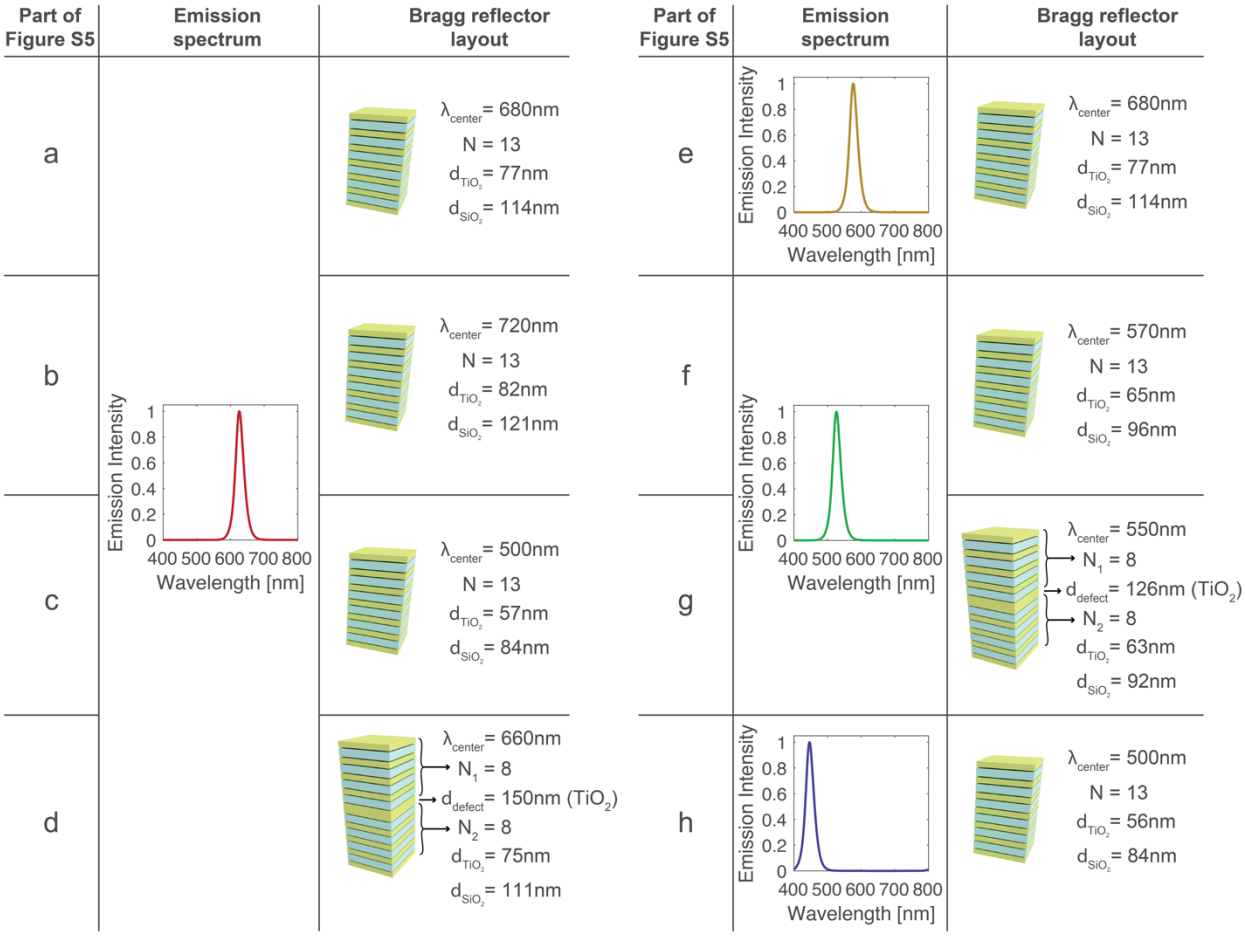

Figure S6**: SLED surface parameters corresponding to the angular emission profiles and Bragg reflector characteristics shown in Fig. S5.** The emission spectrum for each design is shown graphically in the centre columns. The critical Bragg reflector parameters are the reflection peak centre wavelength λ_{center}**,** the number of alternating layers N, and the thicknesses of the individual titania and silica layers d_{TiO_2} and d_{SiO_2}. For the designs in Fig. S5/S6 d, g a half-wave defect layer of titania with thickness d_{defect} is located in the center between to multilayer stacks with layer numbers N_1 and N_2.

References

1. Hopkins, H. H. On the diffraction theory of optical images. *Proc. R. Soc. Lond. Ser. Math. Phys. Sci.* **217**, 408–432 (1953).
2. Born, M. *et al. Principles of Optics: Electromagnetic Theory of Propagation, Interference and Diffraction of Light*. (Cambridge University Press, 1999).
3. Goodman, J. W. *Statistical Optics*. (John Wiley & Sons, 2015).